Journal of Materials Chemistry C

PAPER

View Article Online
View Journal

Cite this: DOI: 10.1039/c8tc06517a

Enhancing charge mobilities in selectively fluorinated oligophenyl organic semiconductors: a design approach based on experimental and computational perspectives†

Buddhadev Maiti, ‡ Kunlun Wang, ‡ Srijana Bhandari, ‡ Scott D. Bunge, * Robert J. Twieg * and Barry D. Dunietz *

Received 24th December 2018,
Accepted 26th February 2019

DOI: 10.1039/c8tc06517a

rsc.li/materials-c

Fluorination can be used to tune optoelectronic properties at the molecular level. A series of oligophenyls with various difluorinations of the phenyl rings has been synthesized, crystalized, structurally resolved and computationally analyzed for charge mobility. We find that difluorination of the phenyl rings at *para* positions leads to oligophenyls that are stacked in symmetrical overlap with significantly enhanced hole mobility as well as the highest electron mobility of the molecules considered. Other difluorinations lead to relatively shifted molecular units in the π-stacked crystal and therefore to lower mobilities. The selectively fluorinated oligophenyls were synthesized using the Suzuki–Miyaura cross coupling reaction. The structures of the products were characterized by X-ray diffraction (XRD), ^{1}H, ^{13}C, ^{19}F NMR spectroscopy and gas chromatography (GC)/mass spectroscopy (MS) measurements. Computational analysis of the materials based on state-of-the-art tools are used to predict their charge transport properties in the crystal phase. In short, we establish a molecular design approach based on fluorination of oligophenyls to achieve enhanced hole mobilities and relatively high electron mobilities.

1. Introduction

Charge mobility plays a crucial role in establishing the performances of devices based on organic semiconducting materials.[1,2] Here we consider an approach to increase charge mobility in crystal films of oligophenyl (OP) derivatives by tuning their properties at the molecular level.[3] Specifically, we study a series of fluorinated oligophenyls that vary in the number of rings and the sites of fluorination.

OPs are widely utilized as molecular building blocks of organic semiconductors and liquid crystals. These materials can be readily synthesized presenting thermal stability and a wide range of electronic and optical properties.[4] For example, *p*-quaterphenyl derivatives have been used as a liquid crystal semiconductor electrode material.[5,6] OPs can be tuned through chemical substitution, and by varying the number of rings.[7–10] Fluorinated liquid crystal materials exhibit rotational viscosity, a broad range of phase transition temperatures and in particular the potential for highly negative dielectric anisotropy essential for display applications.[11,12] Such fluorinated oligophenyls forming liquid crystalline phases include systems with difluoro-substitution of the phenyl precursors.[13]

Systematic introduction of polar C–F bonds in organic semiconducting materials establishes a chemical means to tune the optoelectronic properties of organic semiconducting materials.[14,15] Fluorinated organic molecules have been used as electron transporting materials.[16] Selective fluorination is known to enhance intermolecular attractive interactions[17] resulting in molecules arranged in the solid-state with π stacked arrangements. More recently we showed that symmetrical fluorination where the introduced bond polarities mutually cancel resulting with vanishing dipole enhances charge mobilities in the crystal phase since charge trapping is minimized.[18] In this work, we implement a similar design approach based on a series of fluorinated OPs, which are synthesized, characterized structurally and analyzed computationally to predict their transport properties.

2. Molecular classes

We study a family of OPs with rings bearing two fluorine atoms. Three isomers of di-fluorinated phenyls (DFPs), illustrated in the upper panel of Fig. 1, are used as the building blocks of the OPs.

Department of Chemistry and Biochemistry, Kent State University, Kent, Ohio 44242-0001, USA. E-mail: bdunietz@kent.edu, bunge@kent.edu, twieg@kent.edu

† Electronic supplementary information (ESI) available: Reorganization energies, molecular orbital-based coupling energies, HRFs, normal modes, transport rates, mobilities and atomic coordinates (see in Section 2.4). CCDC 1864595–1864597. For ESI and crystallographic data in CIF or other electronic format see DOI: 10.1039/c8tc06517a

‡ These authors contributed equally to this work.

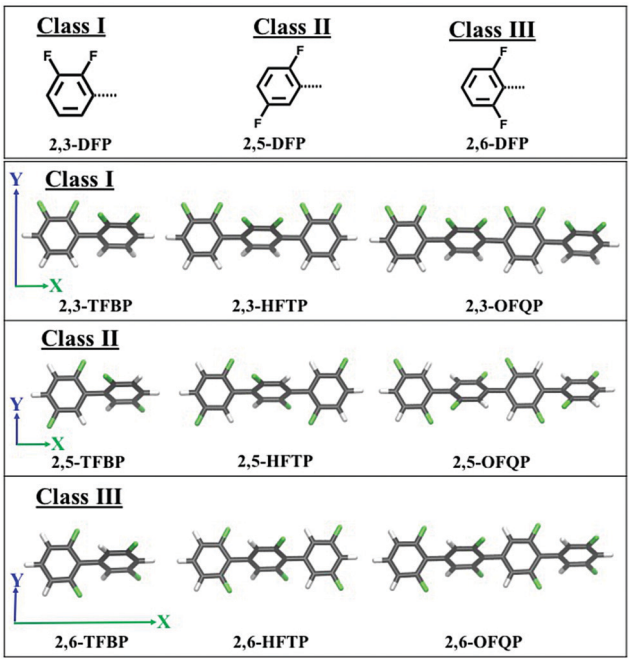

Fig. 1 Three classes of oligomers based on DFP are investigated. The upper panel introduces the different DFP designating the classes. The lower panel shows the conformations of the various OP involving two to four units each. We also provide to the left side of each panel *XY* axis that represent the dipole moment strength of each class. Class I consists of molecules with sizable dipole moments along the molecular width axis (labeled by *Y*; blue): Class II consists of molecules with symmetrical fluorination that leads to vanishing dipole moments. Class III consists of molecules with a large moment along the oligomer main axis (labeled as *X*; green).

Each of the OP series corresponds to one of the considered DFP with up to four rings included. Namely, each series involves tetrafluorobiphenyl (TFBP; two rings), hexafluoroterphenyl (HFTP; three rings), and an octafluoroquaterphenyl (OFQP; four rings); a total of nine materials. The resulting OPs bearing two to four rings are illustrated in the lower panels of Fig. 1, where also shown are the associated trends with regard to the dipole moments of the OPs as follows:

The 2,3-DFP-based ones are with a molecular dipole that is aligned perpendicularly to the oligomer main axis. The dipole moment increases along the OP width (*Y* axis) with the number of rings in spite of the torsional angle between the rings.

The 2,5-DFP-based ones are with a symmetry that leads to a vanishing dipole moment along either of the oligomer axis.

The 2,6-DFP-based ones are with a molecular dipole that is aligned along the oligomer main axis (*X* axis), which increases with the addition of rings and vanishing along the perpendicular axis.

The calculated dipoles along the three axis are listed in Table 1. The quadrupole moment increases with the addition of fluorine atoms and phenyl rings.

3. Experimental approach

The synthesis of the various fluorinated OPs is based on the Suzuki–Miyaura reaction[19] with a different DFP precursor for each series. A detailed description of the synthesis including of the reagents is provided in ESI,† Section 1.1, with a summary of the approach provided next.

Table 1 Dipole moment (unit: Debye) along the oligomer main axis (μ_X), the perpendicular molecular axis (μ_Y), the axis which is perpendicular to the molecular plan (μ_Z) and the quadrupole moments (unit: Debye Å) [see in Fig. 1]

Class	Molecule	μ_X	μ_Y	μ_Z	Q_{xx}	Q_{yy}	Q_{zz}
ωB97X-D/6-31G(d)							
I	2,3-TFBP	0.00	3.88	0.00	−77.46	−84.45	−87.65
	2,3-HFTP	0.00	5.68	0.35	−112.38	−125.46	−132.14
	2,3-OFQP	0.00	7.35	0.01	−149.20	−166.67	−174.99
II	2,5-TFBP	0.00	0.30	0.00	−76.75	−89.34	−88.16
	2,5-HFTP	0.00	0.00	0.00	−112.49	−132.38	−131.86
	2,5-OFQP	0.00	0.31	0.00	−147.46	−176.11	−175.16
III	2,6-TFBP	2.73	0.00	0.00	−74.29	−89.02	−88.81
	2,6-HFTP	4.20	0.00	0.00	−109.28	−132.29	−132.07
	2,6-OFQP	5.68	0.00	0.00	−143.69	−175.50	−175.33
ωB97X-D/cc-pVTZ							
III	2,6-TFBP	2.72	0.01	0.00	−75.86	−90.94	−90.22

The synthesis of the 2,3-DFP based OPs is shown in Fig. 2. The 2,3-difluorophenylboronic acid and 2,3-difluoroiodobenzene were obtained commercially or prepared by the lithiation of 1,2-difluorobenzene at the 3-position followed by the addition of the appropriate electrophile[20] (borate ester or iodine respectively). The 2,3,2′,3′-tetrafluorobiphenyl **1** (2,3-TFBP) was then obtained in 60% yield under standard Suzuki–Miyaura cross coupling conditions. In order to further extend the oligophenyl, the 4′-position next to the fluorine in **1** could also be lithiated just as 2,3-difluorobenzene and the desired monoiodide **2** was obtained in modest yield together with the formation of the diiodide **3**. While the separation of these two iodides (mono : di = 1 : 2 by GC-MS) was not successful, the mixture could be used directly for the subsequent coupling with excess 2,3-difluorophenylboronic acid. The 2,3,2′,3′,2″,3″-hexafluoro-*p*-terphenyl **4** (2,3-HFTP) was isolated from the resulting mixture by extraction with dichloromethane and ethyl acetate in acceptable yield while the quaterphenyl derivative **5** remained in the residue due to its

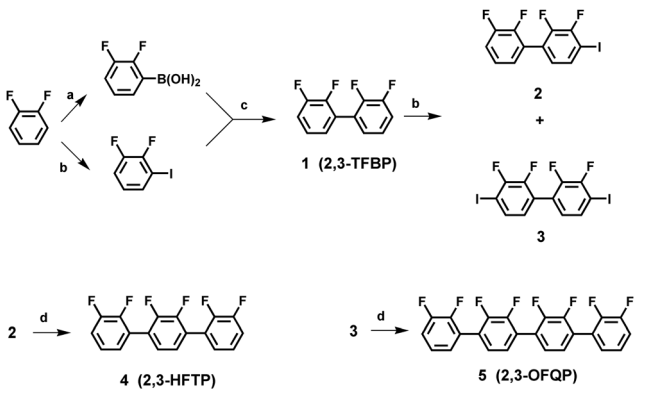

Fig. 2 Synthesis of 2,3-difluorinated oligophenyls and intermediates **1–5**. Reagents and conditions: (a) (i) THF, *n*-BuLi, (ii) $B(OMe)_3$, THF; (b) (i) THF, *n*-BuLi, (ii) I_2, THF; (c) H_2O/1,4-dioxane, $Pd(PPh_3)_4$, K_2CO_3; (d) H_2O/1,4-dioxane, $Pd(PPh_3)_4$, K_2CO_3, 2,3-difluorophenylboronic acid.

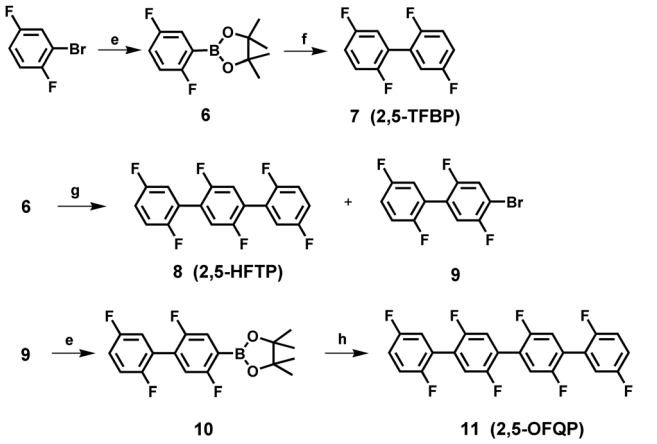

Fig. 3 Synthesis of 2,5-difluorinated oligophenyls and intermediates **7–11**. Reagents and conditions: (e) DMF, KOAc, $Pd(PPh_3)_4$, bis(pinacolato)diboron; (f) 2,5-difluorobromobenzene, H_2O/1,4-dioxane, $Pd(PPh_3)_4$, K_2CO_3; (g) 2,5-difluoro-1,4-dibromobenzene, H_2O/1,4-dioxane, $Pd(PPh_3)_4$, K_2CO_3; (h) **9**, H_2O/1,4-dioxane, $Pd(PPh_3)_4$, K_2CO_3.

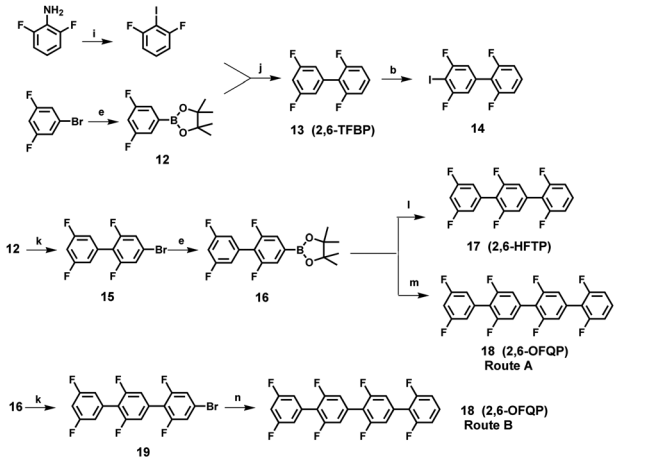

Fig. 4 Synthesis of 2,6-difluorinated oligophenyls and intermediates **12–19**. Reagents and conditions: (b) (i) THF, *n*-BuLi, (ii) I_2, THF; (e) DMF, KOAc, $Pd(PPh_3)_4$, bis(pinacolato)diboron; (i) aqueous HCl, $NaNO_2$, KI; (j) H_2O/1,4-dioxane, $Pd(dppf)Cl_2$, K_2CO_3; (k) 4-bromo-2,6-difluoroiodobenzene, H_2O/1,4-dioxane, $Pd(PPh_3)_4$, K_2CO_3; (l) 2,6-difluoro-1-iodobenzene, H_2O/1,4-dioxane, $Pd(PPh_3)_4$, K_2CO_3; (m) **14**, H_2O/1,4-dioxane, $Pd(PPh_3)_4$, K_2CO_3; (n) potassium 2,6-difluorophenyl trifluoroborate **19b**, H_2O/1,4-dioxane, $Pd(PPh_3)_4$, K_2CO_3.

poor solubility in dichloromethane and ethyl acetate. We then managed to isolate quaterphenyl **5** by extracting the residue with boiling toluene followed by hot filtration of the toluene solution and the desired product crystallized out upon cooling.

The synthesis of the 2,5-DFP based OPs is shown in Fig. 3. As phenylboronic acids bearing multiple fluorine atoms sometimes work poorly in Suzuki coupling due to their electron poor nature (especially when the fluorine is located on a carbon adjacent to the carbon attached to boron), fluorinated pinacolboronic esters were selected for the synthesis of oligophenyls containing the 2,5-difluorophenyl unit. The boronic ester **6** was prepared quantitatively from 2,5-difluorobromobenzene and bis(pinacolato)diboron catalyzed by 0.5–1% palladium tetrakis-(triphenylphosphine).[21] The subsequent Suzuki coupling reaction worked in good yield to give 2,2′,5,5′-tetrafluorobiphenyl **7** (2,5-TFBP). A similar Suzuki reaction was run between 2,5-difluorophenyl pinacolboronic ester (1.2 equivalents) and 1,4-dibromo-2,5-difluorobenzene. In this case the reaction was carefully monitored by TLC and quenched when the starting dibromide was completely consumed and an acceptable amount of the desired monoadduct, 4-bromo-2,5,2′,5′-tetrafluoro-biphenyl **9**, was obtained. The diadduct, 2,5,2′,5′,2″,5″-hexafluoro-*p*-terphenyl **8** (2,5-HFTP) is also a target and was isolated from this same reaction. The bromobiphenyl **9** is a key intermediate for the synthesis of the target quaterphenyl **11**. As before, the bromine in **9** is converted to the pinacolboronic ester **10** and then reacted with **9** to give the final quaterphenyl compound **11**. This large molecule was again isolated and purified by hot filtration/recrystallization from toluene.

The synthesis of 2,6-DFB based OPs is shown in Fig. 4. The 2,2′,6,6′-tetrafluorobiphenyl **13** (2,6-TFBP) was easily prepared beginning with the commercial precursors 2,6-difluoroaniline and 5-bromo-1,3-difluorobenzene in good yield. It turned out that the 4′-position between the two fluorine atoms could be efficiently lithiated[22] and after reaction with iodine the 3,5,2′,6′-tetrafluoro-4-iodobiphenyl **14** was obtained in 91% yield. The 4-bromo-2,3′,5′,6-tetrafluorobiphenyl **15** was prepared from the commercial precursors 2,6-difluorophenylboronic acid and 4-bromo-2,6-difluoro-1-iodobenzene by a highly selective Suzuki coupling reaction at the iodine site. The reactivity of iodine is higher than bromine and by controlling the stoichiometry, the reaction temperature (reflux or lower) and time (normally 2–12 hours), the desired biphenyl bromide **15** could be isolated in modest to good yield (60–80%). Next, 2,6,3′,5′-tetrafluorobiphenyl-4-Bpin **16** was synthesized by a similar method as applied in the earlier set. Suzuki coupling between **16** and relevant iodide proceeded to afford the final terphenyl product **17** and accompanied by the quarterphenyl product **18**. The purification of this molecule was also done by recrystallization from hot toluene. In order to see if **18** could be obtained in better yield, route B also was examined. The terphenylbromide **19** was prepared by a selective Suzuki reaction between **15** and 4-bromo-2,6-difluoro-1-iodobenzene. Here the corresponding 2,6-difluorophenyl potassium trifluoroborate **19b**[23] was utilized instead of the boronic acid, due to the poor reactivity of laterally fluorinated boronic acids according to our experience. Potassium trifluoroborate **19b** worked well and the yield of the Suzuki reaction was improved to 43% (compared to 27% in the first route), which is quite acceptable considering the complexity of the system.

The chemical structure of the synthesized fluorinated oligomers are confirmed by both NMR spectra (see ESI,† Sections 1.2 and 1.3) and mass spectra (see ESI,† Section 1.4). The melting points (MP) of the different crystals including the nonfluorinated OPs are provided in Fig. 5. The melting point increases as the conjugated system is extended as expected from increased intermolecular attractive forces. The 2,3-DFP presents the lowest MP for the three and four rings-based series. The 2,5-DFP is the lowest for the two ring OPs. The 2,6-DFP materials are of the highest MP among the DFP crystals. Lowering of the MP in 2,3-DFP is noted and is explained by noncoplanar arrangement

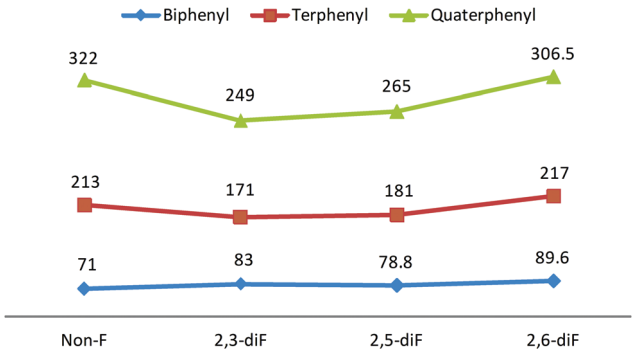

Fig. 5 Melting points, from left to right, of non-F TFBP, 2,3-TFBP, 2,5-TFBP and 2,6-TFBP (°C).

in the crystal reflecting weaker intermolecular attractive forces. In spite of significant effort we have not been able to grow crystals of the terphenyl and quaterphenyl materials of sufficient size and quality to permit determination of their single crystal structures.

4. Computational approach

We proceed next to analyze the charge mobility in the various OPs. We follow our well benchmarked protocol based on a Fermi's golden rule (FGR) theory to calculate charge transfer and transport rate constants.[18,24–27] The fully quantum mechanical FGR rate constants are given by:[28]

$$k_{\mathrm{FGR}} = \frac{|\Gamma|^2}{\hbar^2} \mathrm{e}^{-\sum_\alpha S_\alpha(2n_\alpha+1)} \times \int_{-\infty}^{\infty} \mathrm{d}t F_{\mathrm{r}}^{\mathrm{ex}}(t) \times \exp\left\{-\frac{i}{\hbar}\Delta E t + \sum_\alpha S_\alpha\left[(n_\alpha+1)\mathrm{e}^{-i\omega_\alpha t} + n_\alpha \mathrm{e}^{i\omega_\alpha t}\right]\right\}. \quad (1)$$

Here, Γ is the electronic coupling, $\{\omega_\alpha\}$ are the normal mode frequencies, $\{S_\alpha\}$ are the Huang–Rhys factors (HRFs), and $n_\alpha = \left(\exp\left\{\frac{\hbar\omega_\alpha}{k_{\mathrm{B}}T}\right\} - 1\right)^{-1}$ are the normal mode's thermal occupancies. $F_{\mathrm{r}}^{\mathrm{ex}}(t) = \exp[-k_{\mathrm{B}}TE_{\mathrm{r}}^{\mathrm{ex}}t^2/\hbar^2]$ accounts for outer-shell solvation, where $E_{\mathrm{r}}^{\mathrm{ex}}$ is the corresponding reorganization energy.

Following the high temperature and short time limits, the semiclassical Marcus rate constant can be obtained from the FGR expression[29–32]

$$k_{\mathrm{M}} = \frac{|\Gamma|^2}{\hbar}\sqrt{\frac{\pi}{k_{\mathrm{B}}TE_{\mathrm{r}}}}\exp\left(-\frac{(\Delta E + E_{\mathrm{r}})^2}{4k_{\mathrm{B}}TE_{\mathrm{r}}}\right). \quad (2)$$

The overall reorganization energy is expressed as $E_{\mathrm{r}} = E_{\mathrm{r}}^{\mathrm{ex}} + E_{\mathrm{r}}^{\mathrm{in}}$. The inner-sphere reorganization energy is given by $E_{\mathrm{r}}^{\mathrm{in}} = \sum_\alpha \hbar\omega_\alpha S_\alpha$, where the normal modes are calculated using the OP monomers. ΔE is the energy difference between the donor and acceptor states each at their optimized geometries (see Fig. 6), where for charge transport in a perfect crystal it vanishes.

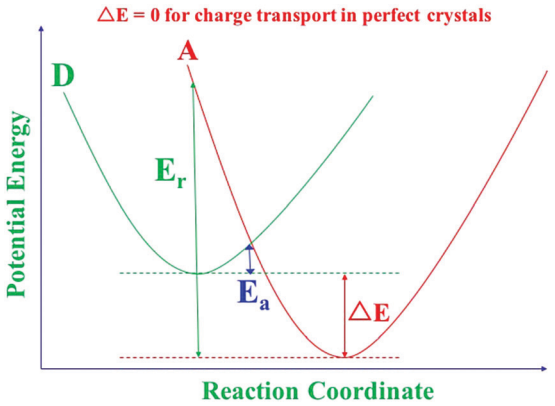

Fig. 6 Scheme of the charge donor (green) and acceptor (red) potential energy surfaces. The key energetic parameters, E_{r}, E_{a} and ΔE are the reorganization energy, activation energy, and energy difference respectively.

Charge mobility in organic crystals, η, is described by the Einstein–Smoluchowski equation:[33]

$$\eta = \frac{eD}{k_{\mathrm{B}}T}, \quad (3)$$

where e, and D indicate the electron charge, and the diffusion constant. Eqn (3) is widely used in studying charge transport in organic crystals.[34–37] In an idealized one-dimensional transport picture, that is also widely employed for simplicity,[34,37] the diffusion constant is evaluated from the rate constant of charge hopping between neighboring molecules:

$$D = a^2k. \quad (4)$$

Here a is the distance between the donor and acceptor molecules, and k is the charge hopping rate constant calculated using a dimer model (evaluated as either k_{M} or k_{FGR}). Therefore the mobilities reported in this study serve as an upper bound to the transport in the crystal that is formally three dimensional. In this way we address below the mobility along the stacking axis for the different oligomers.

Molecular geometries and dimer models are calculated using density functional theory (DFT).[38,39] A range-separated hybrid (RSH) functional[40] ωB97X-D that involves dispersion correction is employed.[41] The ωB97X-D functional was benchmarked well in calculating charge reorganization energies in molecular organic P-type semiconductors,[42] while addressing well the fundamental-gap deficiency that is known to burden the simpler local-density-approximation (LDA)-based functionals.[43–47] Polarizable continuum model (PCM) is used to represent effects of the extended electrostatic environment due to the crystal matrix.[47–49] Clearly transport properties,[47] geometries and reorganization energies are strongly affected by the extended electrostatic environment. For example for 2,3-TFBP gas phase reorganization energies are 0.724 and 1.285 eV for hole and electron transport respectively, whereas with PCM these energies are significantly

smaller at 0.493 and 0.738 eV. The 6-31G(d) basis set is used, where the larger cc-pVTZ basis set values are noted for demonstrating convergence of the calculated properties.

The HRFs are calculated using the DUSHIN program[50,51] by comparing the optimized geometries of the neutral and the charged oligomers. Normal mode frequencies and eigenvectors are obtained using optimized neutral oligomers. Electronic coupling coefficients are calculated using configuration interaction with constrained density functional theory (CDFT-CI).[18,52] In the CDFT calculations, oligomers within an ionic dimer are designated as either the donor or the acceptor of charge to generate the two states used in the CI treatment. For completeness we also compare the dimer based calculated E_r to simpler monomeric based evaluation.

5. Crystal structures

Crystal structures of only the TFBP compounds (**1**, **7** and **13**) are resolved by XRD (see in ESI,† Section 1.5). Dimers of the different TFBPs associated with the strongest attractive intermolecular forces between neighboring molecules are represented in Fig. 7. Our calculated TFBP dimers compare well with intermolecular distances extracted from the resolved XRD structures with a root mean square deviation (RMSD) of only up to 0.3 Å. The RMSD values and key structural features (intramolecular torsional angles and intermolecular distances) are listed in Table 2.

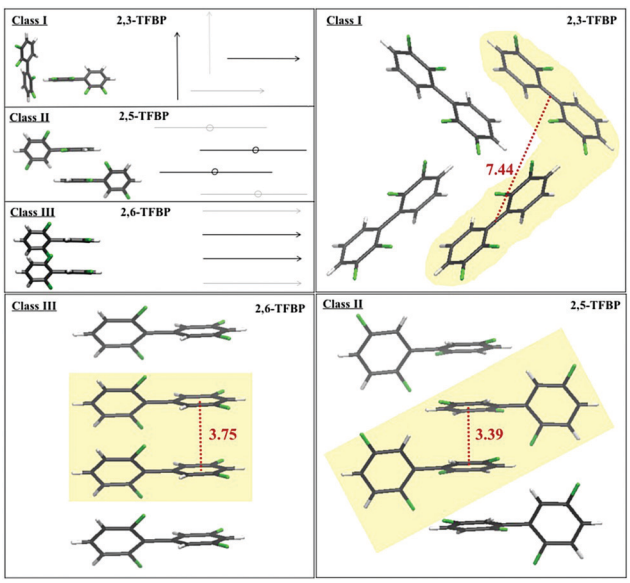

Fig. 7 Class I molecules are arranged in noncoplanar structures, whereas Class II and III molecules are arranged with parallel rings. In Class II the monomers are aligned in alternating directions and with an in-plane relative shift. In Class III the molecules show a cofacial arrangement with optimal overlap of the stacked molecular planes. Dimers extracted from the crystal are shown for 2,3-TFBP (Class I), 2,5-TFBP (Class II) and 2,6-TFBP (Class III). The intermolecular distances are indicated using red-dotted lines (unit: Å): for Class I crystals, the distance between the centers of mass of the monomers is used. For Class II and Class III crystals the distance between two stacked (parallel) phenyl rings is used. The highlighted dimers (yellow b/g) are used below for mobility calculations.

In particular we find:

- Class I crystals based on 2,3-DFP oligomers present a noncoplanar arrangement.[53] The calculated dimer intermolecular distance of 7.43 Å is in agreement with the experimental measured value of 7.44 Å. (The intermolecular separation a is set to the distance between the molecular centers of mass.)
- Class II crystals based on 2,5-DFP oligomers arrange in head-to-tail orientation with a relative longitudinal displacement forming a partial facial overlap.[17,54] The calculated intermolecular distance of 3.35 Å is in agreement with the crystal structure value of 3.39 Å.
- Class III crystals based on 2,6-DFP oligomers are tightly packed in a cofacial arrangement[17] due to substantial attractive intermolecular stacking interactions. The calculated intermolecular distance of 3.64 Å reproduces well the measured value of 3.75 Å.

6. Results and discussion

The key electronic structure parameters for the oligomers are listed in Table 3. We confirm correspondence of the energies of the highest occupied and lowest unoccupied molecular orbitals (HOMO [H] and LUMO [L]) within 0.1 eV of the calculated ionization potential (IP) and the electron affinity (EA), respectively.[47,55]

Intermolecular binding energies F_{inter} of Class I molecules are the smallest with values only up to 1.97 eV, for Class II these increase by 0.2 eV up to 2.16 eV and a substantial further increase for Class III molecules up to 3.08 eV. As expected from the intermolecular energies, Class III molecules exhibit the largest electronic coupling of $\sim$0.20–0.22 eV for hole transport and $\sim$0.08–0.09 eV for electron transport, the coupling values are about one order of magnitude smaller for Class II and even smaller for Class I molecules. The electronic coupling values are listed in Table 3 and Table S2 (see in ESI,† Section 2.1).

The electronic couplings obtained from orbital energies are in good agreement with the CDFT-CI values.[18,52,56] To understand the trend of lower coupling in Class II than those of in Class III we illustrate the HFTP (three ring systems) frontier orbitals in Fig. 8. The lower Class II values appear to result from relative displacement of the OPs.[34,57] The pair of HOMO lobes are oriented along the long molecular axis whereas the LUMOs lobes are oriented along the short molecular axis. Lateral shifts along the long molecular axis result with a larger overlap of the

Table 2 RMSD from crystal structure, ring torsional angle and intermolecular separation of molecular dimers (highlighted in Fig. 7). Measured values are provided in parentheses

Cl.	Molecule	RMSD [Å]	Ring torsional angle [°]	Intermolecular separation [Å]
ωB97X-D/6-31G(d)				
I	2,3-TFBP	0.33	54.50 (56.81)	7.43 (7.44)
II	2,5-TFBP	0.23	55.10 (53.50)	3.35 (3.39)
III	2,6-TFBP	0.23	49.20 (44.95)	3.64 (3.75)
ωB97X-D/cc-pVTZ				
III	2,6-TFBP	0.10	47.60 (44.95)	3.72 (3.75)

Table 3 Frontier orbital energies, ε_H (HOMO) and ε_L (LUMO), are in good agreement with the ionization potential (IP) and the electron affinity (EA), respectively. The intermolecular separation (a) for Class I molecules corresponds to the distance between the molecular centers of mass (c.o.m.), and for Class II and III molecules it is set to the distance between the molecular planes. The intermolecular binding energies (F_{inter}), electronic coupling for hole transport (Γ_h) and electron transport (Γ_e), and hole and electron transport reorganization energy (calculated using dimers, $E_r^{h,d}$, $E_r^{e,d}$ and monomers, ($E_r^{h,m}$), ($E_r^{e,m}$)) reveal significant differences between the three molecular classes

Cl.	Molecule	ε_H [eV]	ε_L [eV]	IP [eV]	EA [eV]	a [Å]	F_{inter} [eV]	Γ_h [eV]	Γ_e [eV]	$E_r^{h,d}$ [eV]	$E_r^{h,m}$ [eV]	$E_r^{e,d}$ [eV]	$E_r^{e,m}$ [eV]
ωB97X-D/6-31G(d)													
I	2,3-TFBP	−8.71	0.76	8.45	−0.40	7.43	−1.07	0.013	0.0045	0.554	0.493	0.741	0.738
	2,3-HFTP	−8.52	0.41	8.16	−0.07	10.02	−1.49	0.00098	0.00041	0.650	0.552	0.709	0.734
	2,3-OFQP	−8.44	0.19	8.02	−0.31	13.06	−1.97	0.0022	0.0012	0.566	0.541	0.710	0.710
II	2,5-TFBP	−8.46	0.65	8.31	−0.30	3.35	−1.31	0.054	0.040	0.534	0.485	0.705	0.724
	2,5-HFTP	−8.35	0.30	8.05	−0.16	3.43	−1.72	0.018	0.021	0.511	0.492	0.648	0.701
	2,5-OFQP	−8.27	0.11	7.93	−0.40	3.41	−2.16	0.0035	0.010	0.561	0.500	0.672	0.642
III	2,6-TFBP	−8.68	0.68	8.41	−0.28	3.64	−1.40	0.216	0.092	0.615	0.557	0.714	0.782
	2,6-HFTP	−8.44	0.27	8.05	−0.24	3.67	−2.28	0.204	0.083	0.638	0.552	0.708	0.766
	2,6-OFQP	−8.33	0.08	7.89	−0.49	3.64	−3.08	0.202	0.086	0.649	0.566	0.678	0.774
ωB97X-D/cc-pVTZ													
III	2,6-TFBP	−8.98	0.44	8.61	−0.03	3.66	−0.51	0.198	0.097	0.671	0.641	0.667	0.762

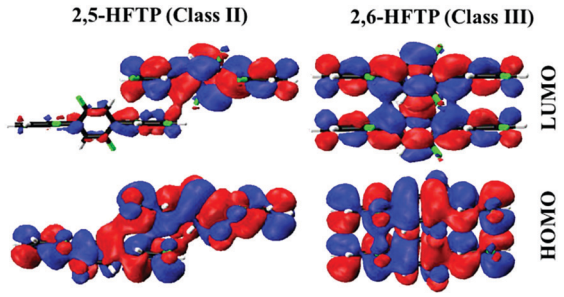

Fig. 8 Frontier orbitals of 2,5-HFTP (left) and 2,6-HFTP (right) dimers. Significant overlap between HOMOs (lower panels) and smaller overlap for LUMOs (upper panels) is indicated. Class III molecules (lower right panel) maintain a substantial cofacial arrangement to increase overlap within the pair of monomer HOMOs (lower left panel).

HOMOs compared to that of the LUMOs. Additional listings of frontier orbital energies and illustrations are provided in the ESI,† Section 2.1.

The reorganization energies E_r tabulated in Table 3 are within the range of 0.4–0.7 eV. Reorganization energies calculated using CDFT dimers are reproduced rather well by simpler ionic monomer calculations, within 0.1 eV in all cases. We therefore proceed to obtain displacement geometries and HRFs based on monomer calculations. Corroborating the harmonic approximation the reorganization energies calculated using the HRFs are in good agreement with their direct evaluation, see ESI,† Section 2.2. In ESI,† Section 2.3 we also provide analysis of the rate constants sensitivity with respect to the external reorganization energy, E_r^{ex}, confirming only marginal influence as expected in a crystal phase.

The modes involved in hole transport are highlighted by following the HRF spectral distribution, see panel (a) of Fig. 9 for 2,6-HFTP. The key low frequency modes are presented in the insets of panel (a) with the mode of 39.86 cm^{-1} illustrated in panel (b) of the figure. This mode appears to result from the relief of steric stress upon depopulation of the monomeric

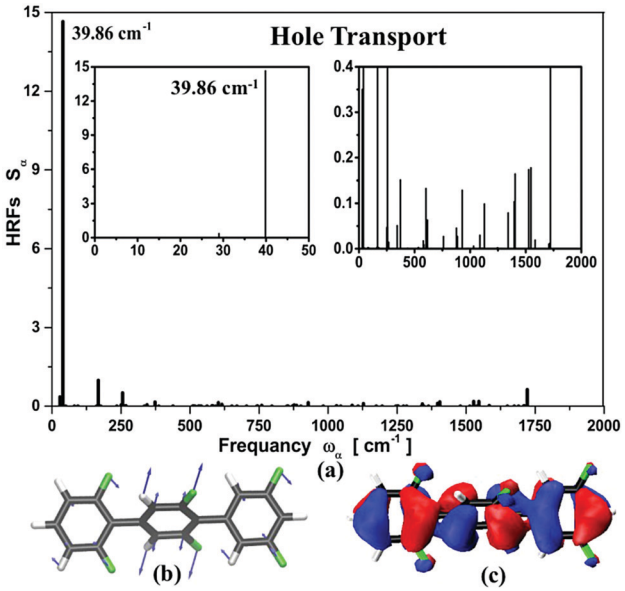

Fig. 9 (a) Huang–Rhys factors (HRFs) for hole transport in 2,6-HFTP. (b) Out-of-plane mode 39.86 cm^{-1} that is associated with the relief of the planar distortion. (c) The monomeric HOMO.

HOMO leading to elongation and contraction of bonds in the bay regions. The HOMO is illustrated in panel (c). Further HRF and frequency distributions are presented in ESI,† Section 2.2.

Hole and electron transport FGR rate constants and mobilities[58,59] at 300 K are listed in Table 4. Importantly, Class I molecules show the lowest charge mobilities with up to 9.1×10^{-2} cm^2 V^{-1} s^{-1} for hole transport in 2,3-TFBP, reflecting weak coupling due to the loose packing. Class II molecules exhibit larger mobilities resulting from the tighter stacking and larger coupling for both hole and electron transport. Here the mobility rises up to 3.1×10^{-1} cm^2 V^{-1} s^{-1} for hole transport in 2,5-TFBP. However, it appears that the lateral shift in Class II materials between adjacent units dampens the coupling and

Table 4 Marcus rate constants, k_M, and charge mobilities, η_M, are up to one order of magnitude smaller than the FGR values k_{FGR} and η_{FGR}. Selective fluorination of Class III results in increased hole and electron mobilities

Molecule	k_M(h) [s^{-1}]	η_M(h) [$cm^2\ V^{-1}\ s^{-1}$]	k_{FGR}(h) [s^{-1}]	η_{FGR}(h) [$cm^2\ V^{-1}\ s^{-1}$]	k_M(e) [s^{-1}]	η_M(e) [$cm^2\ V^{-1}\ s^{-1}$]	k_{FGR}(e) [s^{-1}]	η_{FGR}(e) [$cm^2\ V^{-1}\ s^{-1}$]
ωB97X-D/6-31G(d)								
2,3-TFBP	2.12×10^{10}	4.53×10^{-3}	4.25×10^{11}	9.08×10^{-2}	3.17×10^{8}	6.80×10^{-5}	5.18×10^{9}	1.11×10^{-3}
2,3-HFTP	1.44×10^{8}	5.60×10^{-5}	1.27×10^{9}	4.93×10^{-4}	2.83×10^{6}	1.00×10^{-6}	3.67×10^{7}	1.40×10^{-5}
2,3-OFQP	9.61×10^{8}	6.34×10^{-4}	8.42×10^{9}	5.56×10^{-3}	4.91×10^{7}	3.20×10^{-5}	6.21×10^{8}	4.10×10^{-4}
2,5-TFBP	6.30×10^{11}	2.73×10^{-2}	7.07×10^{12}	3.07×10^{-1}	5.08×10^{10}	2.21×10^{-3}	8.20×10^{11}	3.56×10^{-2}
2,5-HFTP	7.39×10^{10}	3.36×10^{-3}	7.60×10^{11}	3.46×10^{-2}	2.00×10^{10}	9.10×10^{-4}	2.72×10^{11}	1.24×10^{-2}
2,5-OFQP	3.01×10^{9}	1.35×10^{-4}	2.86×10^{10}	1.29×10^{-3}	5.46×10^{9}	2.46×10^{-4}	6.82×10^{10}	3.07×10^{-3}
2,6-TFBP	8.23×10^{12}	4.22×10^{-1}	9.59×10^{13}	4.92×10^{0}	1.23×10^{11}	6.30×10^{-3}	2.09×10^{12}	1.07×10^{-1}
2,6-HFTP	9.80×10^{12}	5.11×10^{-1}	1.07×10^{14}	5.57×10^{0}	1.91×10^{11}	9.95×10^{-3}	2.87×10^{12}	1.50×10^{-1}
2,6-OFQP	8.01×10^{12}	4.11×10^{-1}	7.81×10^{13}	4.00×10^{0}	1.79×10^{11}	9.17×10^{-3}	2.37×10^{12}	1.21×10^{-1}
ωB97X-D/cc-pVTZ								
2,6-TFBP	4.72×10^{12}	2.44×10^{-1}	5.59×10^{13}	2.72×10^{0}	1.36×10^{11}	7.05×10^{-3}	2.31×10^{12}	1.20×10^{-1}

therefore limits the mobility. Class III molecules exhibit the highest electronic coupling and charge mobilities with the largest mobility of 5.6 $cm^2\ V^{-1}\ s^{-1}$ found for hole transport in 2,6-HFTP. Interestingly, the semi-classical values are about one-order of magnitude smaller than the more complete FGR values, demonstrating the importance of the quantum mechanical perspective afforded by FGR even for evaluating charge transport. This trend is in agreement with a recent study of charge transport in related systems.[18]

7. Conclusions

In conclusion, we study three series of oligomers based on 2,3-, 2,5- and 2,6-DFP units, with two to four phenyl rings. All molecules were spectroscopically characterized but crystals only based on two ring compounds were successfully resolved by XRD. We analyzed computationally the effects of the relative orientation of the oligomer units on electronic coupling and hole and electron mobilities. We find that predesigned fluorination of the OP skeleton, at the 2–6 positions, is associated with the largest charge mobility in comparison to the other fluorinations. We find that non-covalent interactions between fluorine and hydrogen contribute to the close-packed crystal structures of the associated Class III molecules. The hole mobility in these oligomers are found to rise up to 5.6 $cm^2\ V^{-1}\ s^{-1}$ for 2,6-HFTP compared to two or three orders of magnitude smaller values for Class II and I materials. The electron mobility follows a similar trend to that of the hole mobility but with overall smaller values. In the case of electron transport we find decreased coupling. The largest electron mobility was found for 2,6-TFBP (0.150 $cm^2\ V^{-1}\ s^{-1}$). We also show that while Marcus rates capture the overall trends, the semiclassical values differ quantitatively from the corresponding FGR values by about one order of magnitude highlighting the need for the more comprehensive treatment.

Conflicts of interest

There are no conflicts to declare.

Acknowledgements

B. D. D. is grateful for support by a NSF-CHE grant CHE-1362504. We are also grateful to generous resource allocations on the Ohio Supercomputer Center[60] and the Kent State University, College of Arts and Sciences Computing Cluster. We thank Dr Suvagata Tripathi for synthetic assistance.

Notes and references

1 M. Muccini, *Nat. Mater.*, 2006, **5**, 605–613.
2 M. Saliba, S. Orlandi, T. Matsui, S. Aghazada, M. Cavazzini, J.-P. Correa-Baena, P. Gao, R. Scopelliti, E. Mosconi and K.-H. Dahmen, *Nat. Energy*, 2016, **1**, 1–7.
3 J. Halls, C. Walsh, N. Greenham, E. Marseglia, R. Friend, S. Moratti and A. Holmes, *Nature*, 2000, **376**, 498–500.
4 X. Fang, S. Domenek, V. Ducruet, M. Refregiers and O. Vitrac, *Macromolecules*, 2013, **46**, 874–888.
5 W.-L. Liau, Y.-J. Su, H.-F. Tseng, J.-T. Chen and C.-S. Hsu, *Liq. Cryst.*, 2017, **44**, 557–565.
6 J. Owen and L. Brus, *J. Am. Chem. Soc.*, 2017, **139**, 10939–10943.
7 H. Yanagi, T. Morikawa, M. Fukushima and T. Mikami, *Synth. Met.*, 2001, **121**, 1613–1616.
8 L. Kong, F. Chesneau, Z. Zhang, F. Staier, A. Terfort, P. Dowben and M. Zharnikov, *J. Phys. Chem. C*, 2011, **115**, 22422–22428.
9 F. Li, W. Chen, K. Yuan and Y. Chen, *Org. Electron.*, 2012, **13**, 2757–2762.
10 L. Ma, Z. Wu, T. Lei, Y. Yu, F. Yuan, S. Ning, B. Jiao and X. Hou, *Org. Electron.*, 2014, **15**, 3144–3153.
11 M. Kašpar, A. Bubnov, V. Hamplová, Z. Málková, S. Pirkl and M. Glogarová, *Liq. Cryst.*, 2007, **34**, 1185–1192.
12 T.-H. Lee, J.-T. Chen and C.-S. Hsu, *Liq. Cryst.*, 2015, **42**, 104–112.
13 N. Aziz, S. M. Kelly, W. Duffy and M. Goulding, *Liq. Cryst.*, 2009, **36**, 503–520.
14 J.-H. Dou, Y.-Q. Zheng, Z.-F. Yao, Z.-A. Yu, T. Lei, X. Shen, X.-Y. Luo, J. Sun, S.-D. Zhang, Y.-F. Ding, G. Han, Y. Yi, J.-Y. Wang and J. Pei, *J. Am. Chem. Soc.*, 2015, **137**, 15947–15956.

15 Z. Tu, X. Huang and Y. Yi, *J. Mater. Chem. C*, 2015, **3**, 1913–1921.
16 J. Calvo-Castro, G. Morris, A. R. Kennedy and C. J. McHugh, *Cryst. Growth Des.*, 2016, **16**, 5385.
17 I. Y. Bagryanskaya, Y. V. Gatilov, A. M. Maksimov, V. E. Platonov and A. V. Zibarev, *J. Fluorine Chem.*, 2005, **126**, 1281–1287.
18 B. Maiti, A. Schubert, S. Sarkar, S. Bhandari, K. Wang, Z. Li, E. Geva, R. J. Twieg and B. D. Dunietz, *Chem. Sci.*, 2017, **8**, 6947–6953.
19 K. W. Quasdorf, M. Riener, K. V. Petrova and N. K. Garg, *J. Am. Chem. Soc.*, 2009, **131**, 17748–17749.
20 A. Chołuj, P. Kula, R. Dabrowski, M. Tykarska and L. Jaroszewicz, *J. Mater. Chem. C*, 2014, **2**, 891–900.
21 J. Lu, Z.-Z. Guan, J.-W. Gao and Z.-H. Zhang, *Appl. Organomet. Chem.*, 2011, **25**, 537–541.
22 T. Rausis and M. Schlosser, *Eur. J. Org. Chem.*, 2002, 3351–3358.
23 G. A. Molander and B. Biolatto, *J. Org. Chem.*, 2003, **68**, 4302–4314.
24 M. H. Lee, E. Geva and B. D. Dunietz, *J. Phys. Chem. C*, 2014, **118**, 9780–9789.
25 M. H. Lee, B. D. Dunietz and E. Geva, *J. Phys. Chem. Lett.*, 2014, **5**, 3810–3816.
26 A. K. Manna and B. D. Dunietz, *J. Chem. Phys.*, 2014, **141**, 121102.
27 M. H. Lee, E. Geva and B. D. Dunietz, *J. Phys. Chem. A*, 2016, **120**, 2970–2975.
28 A. Nitzan, *Chemical Dynamics in Condensed Phases: Relaxation, Transfer and Reactions in Condensed Molecular Systems: Relaxation, Transfer and Reactions in Condensed Molecular Systems*, Oxford University Press, 2006.
29 R. A. Marcus, *J. Chem. Phys.*, 1956, **24**, 966–978.
30 R. A. Marcus, *J. Chem. Phys.*, 1956, **24**, 979–989.
31 R. A. Marcus and N. Sutin, *Biochim. Biophys. Acta*, 1985, **811**, 265–322.
32 R. A. Marcus, *Rev. Mod. Phys.*, 1993, **65**, 599–610.
33 G. L. Hornyak, J. Dutta, H. F. Tibbals and A. Rao, *Introduction to nanoscience*, CRC Press, 2008.
34 V. Coropceanu, J. Cornil, D. A. da Silva Filho, Y. Olivier, R. Silbey and J.-L. Brédas, *Chem. Rev.*, 2007, **107**, 926–952.
35 G. R. Hutchison, M. A. Ratner and T. J. Marks, *J. Am. Chem. Soc.*, 2005, **127**, 2339–2350.
36 G. Nan, X. Yang, L. Wang, Z. Shuai and Y. Zhao, *Phys. Rev. B: Condens. Matter Mater. Phys.*, 2009, **79**, 115203.
37 S. Yin, L. Li, Y. Yang and J. R. Reimers, *J. Phys. Chem. C*, 2012, **116**, 14826–14836.
38 P. Hohenberg and W. Kohn, *Phys. Rev.*, 1964, **136**, B864.
39 W. Kohn and L. J. Sham, *Phys. Rev.*, 1965, **140**, A1133.
40 R. Baer and D. Neuhauser, *Phys. Rev. Lett.*, 2005, **94**, 043002.
41 J.-D. Chai and M. Head-Gordon, *Phys. Chem. Chem. Phys.*, 2008, **10**, 6615–6620.
42 C. Bruckner and B. Engels, *J. Comput. Chem.*, 2016, **37**, 1335–1344.
43 E. Livshits and R. Baer, *Phys. Chem. Chem. Phys.*, 2007, **9**, 2932–2941.
44 T. Stein, L. Kronik and R. Baer, *J. Am. Chem. Soc.*, 2009, **131**, 2818–2820.
45 L. Kronik, T. Stein, S. Refaely-Abramson and R. Baer, *J. Chem. Theory Comput.*, 2012, **8**, 1515–1531.
46 H. Phillips, E. Geva and B. D. Dunietz, *J. Chem. Theory Comput.*, 2012, **8**, 2661–2668.
47 H. Phillips, Z. Zheng, E. Geva and B. D. Dunietz, *Org. Electron.*, 2014, **15**, 1509–1520.
48 J. Tomasi, B. Mennucci and R. Cammi, *Chem. Rev.*, 2005, **105**, 2999–3094.
49 J.-M. Mewes, Z.-Q. You, M. Wormit, T. Kriesche, J. M. Herbert and A. Dreuw, *J. Phys. Chem. A*, 2015, **119**, 5446–5464.
50 J. R. Reimers, *J. Chem. Phys.*, 2001, **115**, 9103–9109.
51 J. Tang, M. T. Lee and S. H. Lin, *J. Chem. Phys.*, 2003, **119**, 7188–7196.
52 Q. Wu, B. Kaduk and T. Van Voorhis, *J. Chem. Phys.*, 2009, **130**, 034109.
53 D. Cruickshank, *Acta Crystallogr.*, 1957, **10**, 504–508.
54 F. Cozzi, S. Bacchi, G. Filippini, T. Pilati and A. Gavezzotti, *Chem. – Eur. J.*, 2007, **13**, 7177–7184.
55 E. J. Baerends, O. V. Gritsenko and R. van Meer, *Phys. Chem. Chem. Phys.*, 2013, **15**, 16408–16425.
56 Q. Wu and T. V. Voorhis, *J. Chem. Phys.*, 2006, **125**, 164105.
57 J.-L. Brédas, J. P. Calbert, D. A. da Silva Filho and J. Cornil, *Proc. Natl. Acad. Sci. U. S. A.*, 2002, **99**, 5804–5809.
58 A. Troisi, *Adv. Mater.*, 2007, **19**, 2000–2004.
59 C. R. Kagan and C. B. Murray, *Nature*, 2015, **10**, 1013–1026.
60 Ohio Supercomputer Center, 1987, http://osc.edu/ark:/19495/f5s1ph73.

